Chapter 7: Signature of Skyrmions and Evidence for the Local Noncentrosymmetric Crystal Structure in Hexagonal NiMnGa

In the present chapter, we provide the detection of skyrmions with hysteretic character by magnetic field dependent ac-susceptibility data and propose the first evidence of local noncentrosymmetric crystal structure in the average centrosymmetric hexagonal NiMnGa by atomic pair distribution function study using high-*Q* synchrotron x-ray powder diffraction data.

7.1 Introduction

The last decade is the witness of enormous interest in an exotic class of noncollinear magnetic textures known as skyrmions, which is the particle-type swirling of magnetic spins around the unit sphere in the nanometer scale [178, 232, 339]. Magnetic skyrmions received vast attention due to their developing capability in the high-density information carriers, data processing, and memory devices [162, 171-174]. These important technological applications are owned by the unique properties of skyrmions for e.g., nanometer size, topological stability, and low current density (~ 10^5–10^6 A-m^{-2}) required to drive the skyrmion textures [175-177]. There are very limited experimental techniques that have been known until the date for the detection of magnetic skyrmions. Some of them are Lorentz transmission electron microscopy (L-TEM) [187], small angle neutron scattering (SANS) [187], electron holography [194], heat capacity [400], and magnetotransport measurements [187]. These sophisticated experimental techniques are complicated and not easily available to users. In addition, there are some limitations as well for e.g., heat capacity would not be useful for high-temperature skyrmions detection due to unavoidable phonon contribution at higher temperature [194]. Therefore, easily available experimental techniques are demanded over time to detect magnetic textures of skyrmion. Recently, the magnetic field and frequency-dependent ac-magnetization measurement have

emerged as an excellent technique for detecting the skyrmions, magnetic relaxation, etc. [188, 194, 401, 402]

After the discovery of skyrmions in MnSi [178], the observation of skyrmions was limited to the noncentrosymmetric materials for e.g., B20 magnets like MnSi [178], MnGe [179], FeGe [180], Cu_2OSeO_3 [181]; due to the competition between Heisenberg exchange interactions and Dzyaloshinskii-Moriya interactions (DMI) [182, 183]. Subsequently, the skyrmions were also discovered in the centrosymmetric materials having inversion symmetry [11, 185, 186] for e.g., layered manganite ($La_{2-2x}Sr_{1+2x}Mn_2O_7$) [185], NiMnGa [187], NiI_2 [189], Ni_2MnGa [11], Ni-Mn-In [83], etc. The presence of magnetocrystalline anisotropy (MCA) plays an important role in the stabilization of skyrmions via frustrated or competing magnetic interactions between magnetic anisotropy energy and dipole-dipole interactions energy in the centrosymmetric materials [11, 185, 187, 188, 214, 403].

Recently, among a different kinds of existing skyrmions [232], biskyrmion received great attention due to their size and topological charge tunability using the thickness, magnetic field, and electrical current [188]. Biskyrmions are a set of two individual skyrmions with opposite helicities [188]. Earlier, biskyrmions were observed in the centrosymmetric materials having strong uniaxial magnetic anisotropy or MCA for e.g. $La_{2-2x}Sr_{1+2x}Mn_2O_7$ [185], NiMnGa [187], and MnPdGa [188]. More recently, it has also been reported in the noncentrosymmetric chimney ladder compound $Cr_{11}Ge_{19}$ [404]. This suggests the inversion symmetry is not a necessary condition to the formation of biskyrmions, wherein the absence of rotational symmetry enables to utilize a rotation of biskyrmions in spintronic devices [405]. Further, the absence of rotational symmetry in the biskyrmions reduces the skyrmion Hall effect, which is an ongoing problem in the making of spintronic-based devices [405].

Among different biskyrmions hosting materials, hexagonal NiMnGa emerges as a potential candidate as it exhibits superstable biskyrmion textures in the wide temperature range (16-340 K) [187, 378] and high value of FM T_C ~ 350 K [187, 213, 214, 378]. The hexagonal NiMnGa requires a comparatively small magnetic field to induce the biskyrmion textures at room temperature and can be stabilized even at zero magnetic field using field cooling protocol [187, 378]. It exhibits a uniaxial magnetic easy axis along *c*-direction below the FM T_C and noncollinear spin configuration with FM to spin orientation transition in the form of spin canting [214, 395]. The magnetic properties of NiMnGa can be easily modified by compositional tuning [214, 380]. Earlier, the crystal structure of PtMnGa, which is a sister compound of NiMnGa, was thought to be hexagonal in the centrosymmetric $P6_3/mmc$ space group [234]. Recently, selected-area electron diffraction and single crystal x-ray diffraction studies revealed that the structure of PtMnGa is trigonal in the $P3m1$ space group, which is noncentrosymmetric [209]. This explains the formation of Neel-type skyrmions in PtMnGa [209]. More recently, Cooley *et al.*, observed no evidence of $P3m1$ space group in the average structure of PtMnGa using synchrotron x-ray diffraction and neutron powder diffraction [45]. Moreover, selected-area electron diffraction may provide the information at the local scale [46]; it is necessary to investigate the local structure of related sister compounds. This motivated us to perform a detailed local structure investigation of hexagonal NiMnGa. We believe that an investigation of short-length scale correlations can provide microscopic insight into the origin of skyrmions in such systems.

Local symmetry breaking or structural disorder without long-range ordering in crystalline materials may provide a vital improvement in the exotic physical properties, which can be directly utilized in the technology [235]. Local environments dictate the various physical phenomena for e.g., local defects and disorder have a strong impact on the critical temperature in the

superconductors [235]; local ferroelectricity generated by off-centering of atoms results to reduce the thermal conductivity, which enhance the figure of merit in thermoelectric materials [406, 407]; local disorder can be used to optimize the electrical properties of lead zirconate titanate perovskite [408]; formation of polar nano-regions (PNRs) entitle to understand the dielectric properties in the relaxor ferroelectrics [306, 307]; distinct electronic properties in $SrTiO_3$ and $BaTiO_3$ [409]; colossal magnetoresistance in the manganite [235], short-range ordered lattice of quantum dots [235], nano-catalyst whose performance dependents on short-range structure [235], local defects and cation disorder are optimized to achieve the performance of the cathode materials used for energy storage [235], skyrmions via premartensite phase which can exist locally [64, 83], etc. Local structure study enables us to understand the impact of the local disorder on various physical properties and phenomena mentioned above [235, 408, 410-412].

In this chapter, we present the hysteretic behavior of skyrmions and evidence of local noncentrosymmetric structure in NiMnGa alloy. The magnetic field-dependent ac-susceptibility data analysis provides unambiguous hysteretic behavior of skyrmions formation with field stable down to the 5 K. Temperature dependent ac-susceptibility data provides the magnetic phase transitions. Rietveld refinements using high-*Q* PDF data reveal the long-range (LR) hexagonal ($P6_3/mmc$) structure remains unchanged with a change in temperature in the 400-100 K range. The PDF analysis suggests that although anisotropic atomic displacement parameters (ADPs) consideration provides a better fit than the isotropic ADPs, the large value of anisotropic ADPs observed in the short-range (SR) at all the respective temperatures. A careful investigation in the SR unleashes the presence of noncentrosymmetric trigonal structure in the $P3m1$space group. This result opens a new pathway to revisit the origin of skyrmions in the centrosymmetric materials.

7.2 Experimental Section

Details of the sample preparation, phase purity confirmation and compositional study of NiMnGa are described in the section 6.2. The temperature dependent ac-susceptibility ($\chi(T)$) at a drive field 10 Oe for 333.33 Hz frequency was collected during the warming cycle on zero-field cooled sample using a SQUID-VSM (Quantum Design, MPMS). In addition, the field-dependent ac-susceptibility ($\chi(H)$) measurements were carried out under zero-field cooled protocol i.e., for each temperature, the sample was cooled from its paramagnetic phase under zero magnetic field using a VSM option of PPMS (Quantum Design). The temperature dependent (100-400 K) synchrotron x-ray powder diffraction (SXRPD) measurements were carried out in high-Q mode using high flux and high energy x-rays with a wavelength (λ) of 0.20742 Å at P02.1 beamline at PETRA-III DESY, Germany [246]. The borosilicate capillaries were used as a sample container for the SXRPD measurements. The high-Q measurements were performed with a maximum instrumental Q-value ($Q_{maxinst}$) of 23 $Å^{-1}$. The high-Q SXRPD data was also collected of empty borosilicate capillary required for the background subtraction.

7.3 Results and Discussion

7.3.1 Temperature Dependent AC-Susceptibility

The temperature dependence of the real part of ac-susceptibility ($\chi'(T)$) is shown in Figure 7.1. On lowering the temperature, the sudden increase in $\chi'(T)$ around 350 K corresponds to the paramagnetic phase to ferromagnetic (FM) phase transition. The value of FM transition temperature T_C ~ 350 K is close to the onset of the rising part of $\chi'(T)$ and is in good agreement with that reported in the literature [187]. Besides FM T_C, the appearance of rapid decrement in $\chi'(T)$ on going below 210 K is due to the presence of spin reorientation transition (SRT) [214]. The SRT temperature was found to be T_{SRT} ~ 200 K as calculated by temperature derivative of $\chi'(T)$.

The rapid decrease in $\chi'(T)$ below 50 K is a matter of future investigation (see Figure 7.1). The present behavior of $\chi'(T)$ and magnetic transition temperatures are in good agreement with the previous report [214] and with the low field magnetization given in Figure 6.2(a) of section 6.3.1.

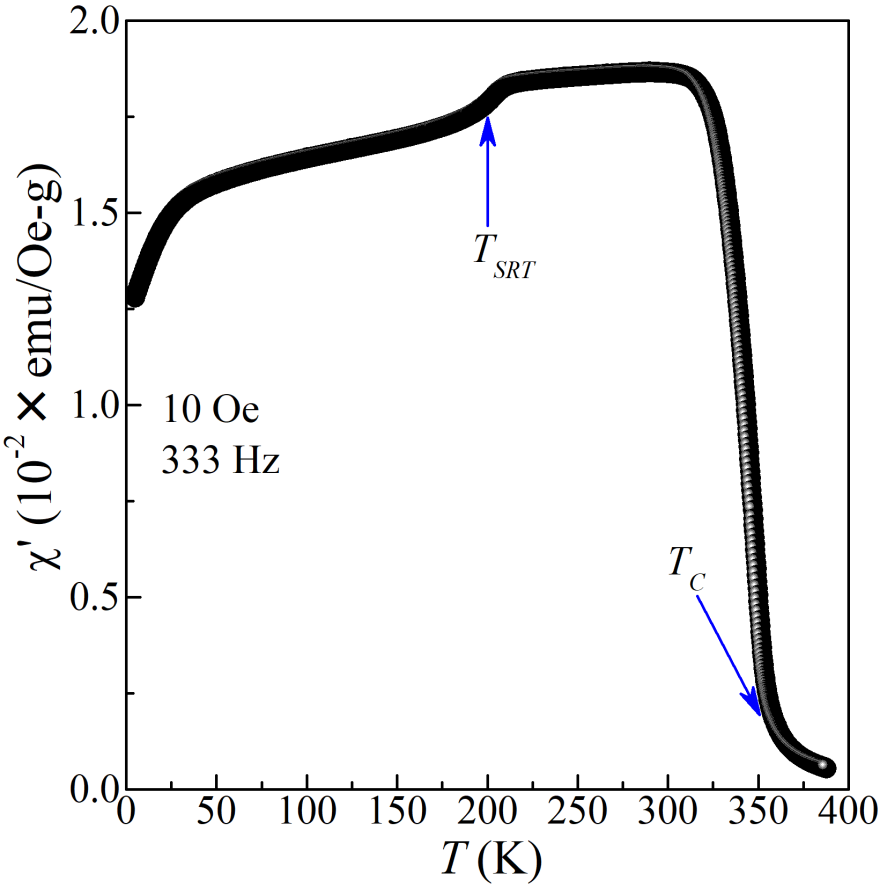

Figure 7.1: Temperature dependence of the real part of ac-susceptibility ($\chi'(T)$) of NiMnGa, measured at 333 Hz under the zero-field cooled warming cycle. The T_C and T_{SRT} indicate the ferromagnetic and spin reorientation transition temperature, respectively.

7.3.2 Signature of the Skyrmions with Hysteretic Nature using Magnetic Field Dependent AC-Susceptibility Measurements

It is necessary to confirm the presence of skyrmions in the present sample of NiMnGa before moving to their origin. Apart from several techniques, the magnetic field-dependent ac-susceptibility ($\chi(H)$) measurement has been found as an excellent technique to detect the skyrmions [188, 194, 401, 402] as discussed in the introduction part (see section 7.1). Therefore, we carried out $\chi(H)$ measurements at different temperatures of NiMnGa to capture the signatures of skyrmions. Figure 7.2(a) shows the variation of the real component of ac-susceptibility data (χ') with dc magnetic field (H) (χ' *vs* H plot) at 220 K in increasing and decreasing field in the range of -1 T to 1 T. The temperature 220 K was selected because the maximum density of biskyrmion domains has been reported around 215 K for NiMnGa using L-TEM [187]. The χ' *vs* H plot exhibits peak like feature around $\pm$0.25 T and $\pm$0.5 T of the magnetic field indicated by two critical magnetic fields H_S and H_C, respectively (marked by the blue and black arrow in Figure 7.2(a)). The helical to biskyrmion state and biskyrmion to FM phase transition occurs at H_S and H_C, respectively. These critical fields are in good agreement with L-TEM results for the present system [187]. The transition among different magnetic textures of skyrmions at the critical fields has also been reported in the sister compound (MnPdGa) [188]. To get more insight, the field derivative of χ' around the critical fields has been demonstrated in Figure 7.2(b). The insets (i) & (ii) of Figure 7.2(b) show an enlarged view around -0.25 T and +0.25 T value of the field, respectively. The insets (i) & (ii) of Figure 7.2(b) reveal the small hysteretic behavior of biskyrmion formation field (H_S) as the value of H_S (maxima and minima in insets (i) & (ii)) are not the same (slightly shifted) during increasing and decreasing field. Such hysteresis feature in skyrmionic transition also has been reported for Mn-Pt(Pd)-Sn system [194]. These results provide the signature of biskyrmion

formation with magnetic field and its hysteretic behavior indicate that they formed on the nucleation and growth principle i.e., helical to biskyrmions transition in NiMnGa is analogous to weakly-first-order in character.

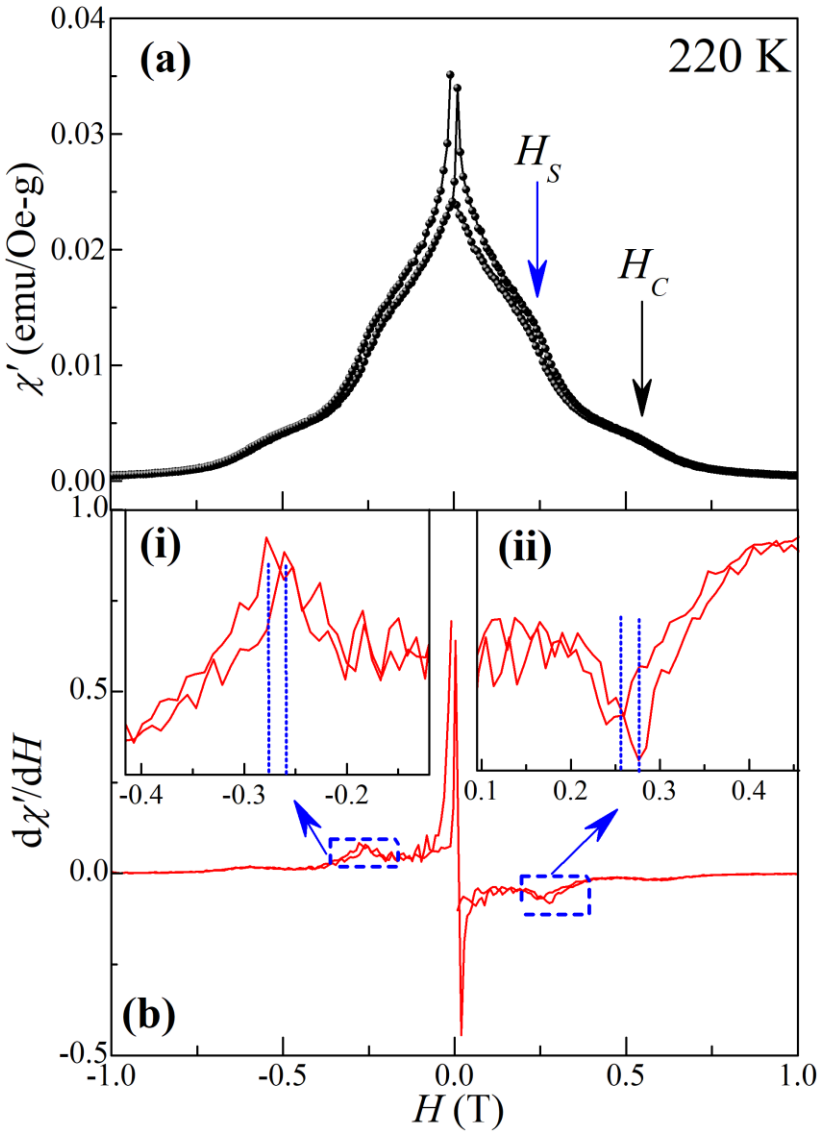

Figure 7.2: (a) The variation of the real component of ac-susceptibility (χ') with dc magnetic field (H) (χ' *vs* H plot) at 220 K with increasing and decreasing field (-1 T to 1 T). H_S and H_C indicate the critical fields at which the system transforms from helical to biskyrmions and from biskyrmions to ferromagnetic states, respectively. (b) The first derivative (dχ'/dH) of χ' vs H plot. The insets (i)

& (ii) of (b) depict an enlarged view around -0.25 T and 0.25 T, respectively, where the vertical dashed lines indicate the increasing and decreasing fields of maxima and minima.

Moreover, the stability of biskyrmion in NiMnGa has been reported in the large temperature range of 16-340 K using L-TEM [187, 378]. Due to added advantage of χ measurement using PPMS, we could abled to collect the χ' *vs* H data in the temperature range of 5 to 370 K. For comparison, besides 5 K, the other temperatures for the measurements were selected using temperature at which Hall resistivity data has been reported by W. Wang *et. al* [187]. The χ' *vs* H data were collected on the zero-field cooled sample at the selected temperatures. The data were collected with increasing as well as a decreasing field (-1 T to 1 T) since the field cooled procedure may affect the density of biskyrmions as reported for present NiMnGa [378]. For the sake of representation, Figure 7.3 shows χ' *vs* H plot at different temperatures (5 to 340 K) in increasing magnetic field only (0 to $\pm$1 T) only. Note that the χ' *vs* H plot at 370 K does not exhibit any signature of spin texturing effect and behave like simple paramagnetic phase as FM T_C ~ 350 K observed in $\chi'(T)$ (Figure 7.1) and hence not included here. Figure 7.3 unleashes the double peak behavior (around H_S and H_C) in positive as well as negative fields present at all measured temperatures and peaks ~0.28 T and ~0.58 T persist up to 5 K. This suggests that the biskyrmion textures are stable down to 5 K. It is worth to note that the intensity of peak got diminished at 340 K, which is certainly due to closeness of the measured temperature to T_C (~350 K). The value of H_S and H_C and corresponding peak intensity gets enhanced by lowering the temperature. The inset of Figure 7.3 shows the enlarged view around 0.2 T wherein the increasing behavior of critical magnetic field (H_S) and peak growth on decreasing the temperature is guided by the blue arrow. A careful inspection of this inset reveals that the peak intensity gets enhanced up to 220 K, and below that, the peak intensity seems to get broadened. This is a probable indication of the maximum density of biskyrmion spin textures since

the maximum value of topological hall resistivity and biskyrmions density ~215 K has been reported for NiMnGa [187]. The enhancement of critical fields has also been reported for NiMnGa using L-TEM [187, 378]; therefore, our results are in good agreement with the literature. In brief, the field-dependent ac-susceptibility data analysis provides evidence for the hysteretic nature of biskyrmion state that is stable down to 5 K.

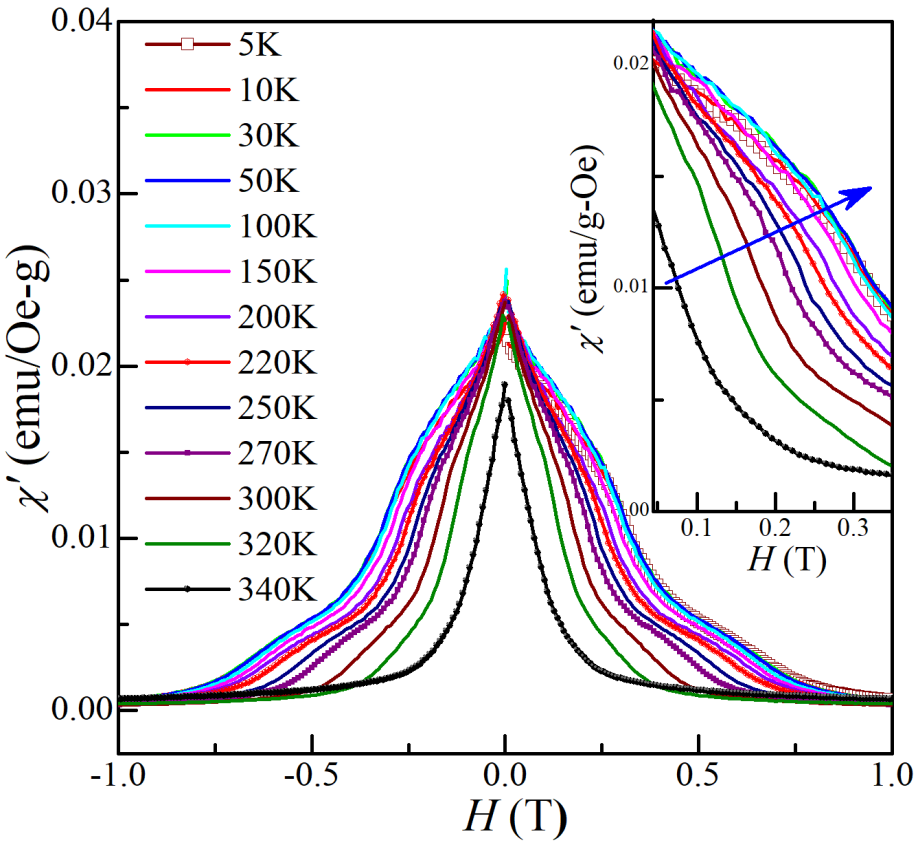

Figure 7.3: The variation of the real component of ac-susceptibility (χ') with dc magnetic field (H) (χ' *vs* H plot) at the indicated temperatures (5 to 340 K) with increasing magnetic field only (0 to $\pm$1 T). The inset shows the enlarged view around 0.2 T. The blue arrow in the inset indicates the increasing behavior of critical field (H_S) and peak growth on decreasing the temperature.

After confirming the presence of biskyrmions, we move toward their origin in NiMnGa. In order to investigate that, the atomic pair distribution function method was opted for local structure study of NiMnGa using high-*Q* SXRPD data as described in the following section.

7.3.3 Temperature Dependent High-*Q* Synchrotron X-ray Powder Diffraction

The average long-range ordered crystal structure was determined by the Rietveld refinements [298]. The refinement was carried out using the FULLPROF package [299] in the hexagonal $P6_3/mmc$ space group considering all the atoms at the special Wyckoff positions, i.e., Mn at 2a (0, 0, 0), Ni at 2d (1/3, 2/3, 3/4), and Ga at 2c (1/3, 2/3, 1/4), respectively [187, 214]. The Rietveld refinements were carried out using high-*Q* SXRPD patterns collected in the temperature range of 400-100 K. The results of the Rietveld refinement at 400 K, 300 K, and 100 K are shown in Figure 7.4(a), (b), and (c), respectively, which show an excellent fit between the observed and calculated peak profiles by accounting for all the Bragg peaks. This suggests the average hexagonal structure with the $P6_3/mmc$ space group in the 400-100 K range. The parameters obtained after the Rietveld refinements at the selected temperature (400 K, 300 K, and 100 K), covering both magnetic transitions (T_C ~ 350 K and T_{SRT} ~ 200 K), is shown in Table 7.1. The reduced structure function *F(Q)*, obtained from the high-*Q* SXRPD patterns (shown in Figure 7.4(a), (b), and (c)), is depicted in Figure 7.4(d), (e), and (f) at 400 K, 300 K, and 100 K, respectively. The details of *F(Q)* conversion from high-*Q* SXRPD pattern are described in section 3.2. We note that the intensity of the peaks in the *F(Q)* diminishes significantly towards higher *Q* values suggesting the dominance of the diffuse scattering. Also, the intensity of the peaks in the *F(Q)* diminishes quickly with *Q* at 400 K compared to 100 K. This attributes to the effect of the thermal broadening.

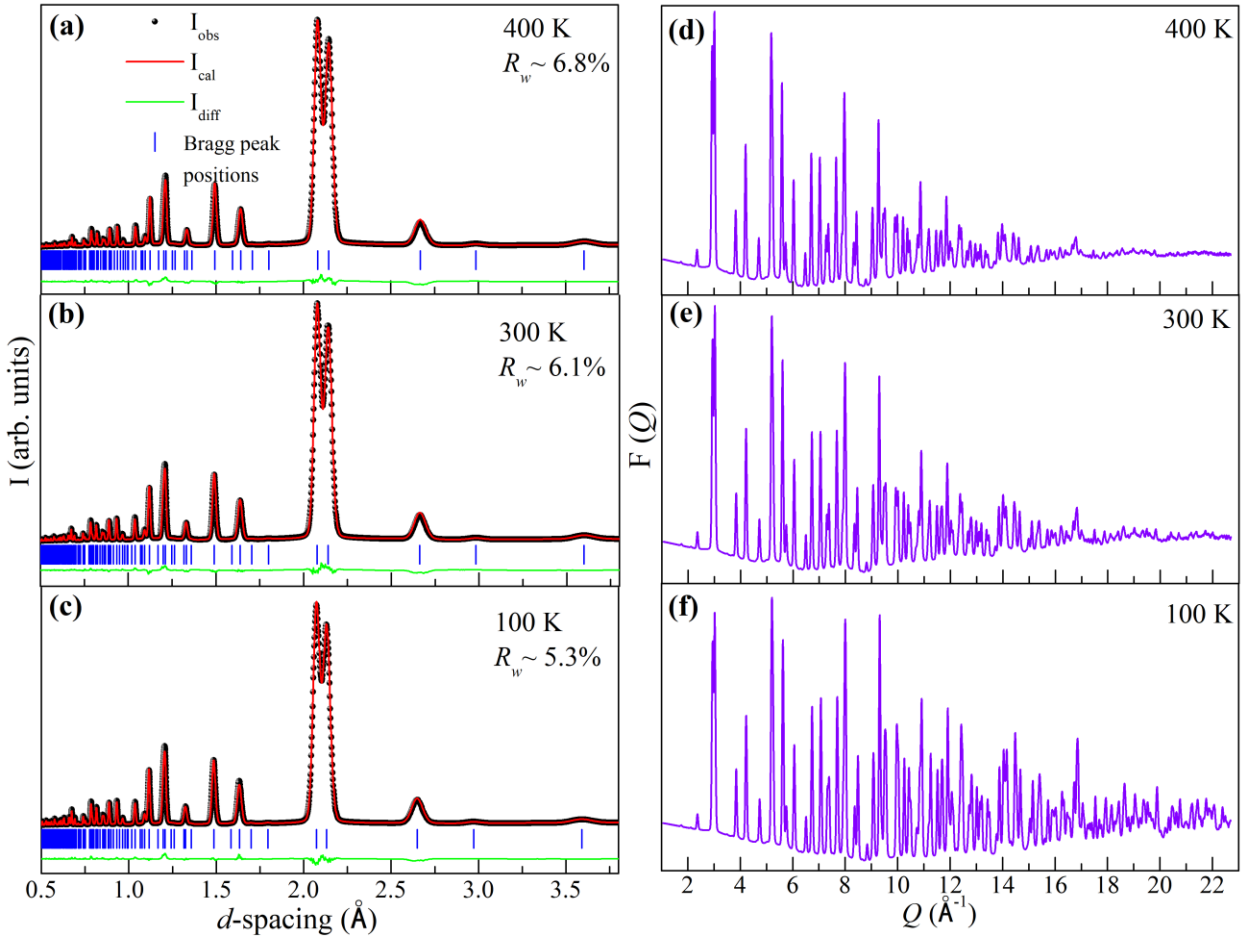

Figure 7.4: The observed profile (black spheres), calculated profile (continuous red line), difference profile (continuous green line), Bragg peak positions (blue ticks), and weighted agreement factor (R_w) obtained after Rietveld refinement in the $P6_3/mmc$ space group of NiMnGa using high-Q synchrotron x-ray powder diffraction data at (a) 400 K, (b) 300 K, and (c) 100 K. The reduced structure function F(Q) vs Q at (d) 400 K, (e) 300 K, and (f) 100 K.

Table 7.1: The lattice parameters (*a* and *c*), thermal factor (B), and agreement factors obtained after Rietveld refinement (with $P6_3/mmc$ space group) using temperature dependent high-*Q* SXRPD data of NiMnGa.

Temperature → Parameters ↓	**400 K**	**300 K**	**100 K**
a (Å)	4.16220(5)	4.15552(4)	4.14569(2)
c (Å)	5.33731(9)	5.32476(8)	5.29734(6)
B_{Ni} (Å^2)	0.82(2)	0.63(1)	0.37(1)
B_{Mn} (Å^2)	0.508(6)	0.401(5)	0.202(3)
B_{Ga} (Å^2)	1.01(1)	0.73(1)	0.26(1)
R_p	6.34	5.67	4.79
R_{wp}	6.85	6.13	5.32

7.3.4 Temperature Dependent Atomic Pair Distribution Function Analysis

The conventional Rietveld refinement enables to determine the average long-range ordered (LRO) structure based on the Bragg peaks only. It ignores the diffuse scattering and, hence, cannot capture the deviations from the average LRO structure at short length scales of the order of one to a few unit cells, which contribute to the diffuse scattering. We opted the atomic pair distribution function (PDF) [270-273] technique to explore both the short-range ordered (SRO) and LRO structure together, using high flux, high energy, and high-*Q* SXRPD data. The beauty of PDF provides the information in the SR (SR; within the unit cell), medium-range (MR; limited to a few unit cells), and long-range (LR; above the medium range in the real-space) regimes simultaneously [306, 307]. The details of atomic PDF conversion are described in section 3.2. The scattering structure

function *S(Q)* and experimental reduced atomic PDF *G(r)* in the temperature range of 100-400 K were obtained from the high-*Q* (Q_{max} = 22.7 Å^{-1}) SXRPD using the PDFgetx3 program [273]. The PDF refinements were carried in the direct space using the program PDFgui [274]. Since the present PDF data were collected using high energy (60 keV) synchrotron x-rays in the transmission mode, the x-rays could penetrate through the powder sample in the sample holder and provide information about the bulk behavior.

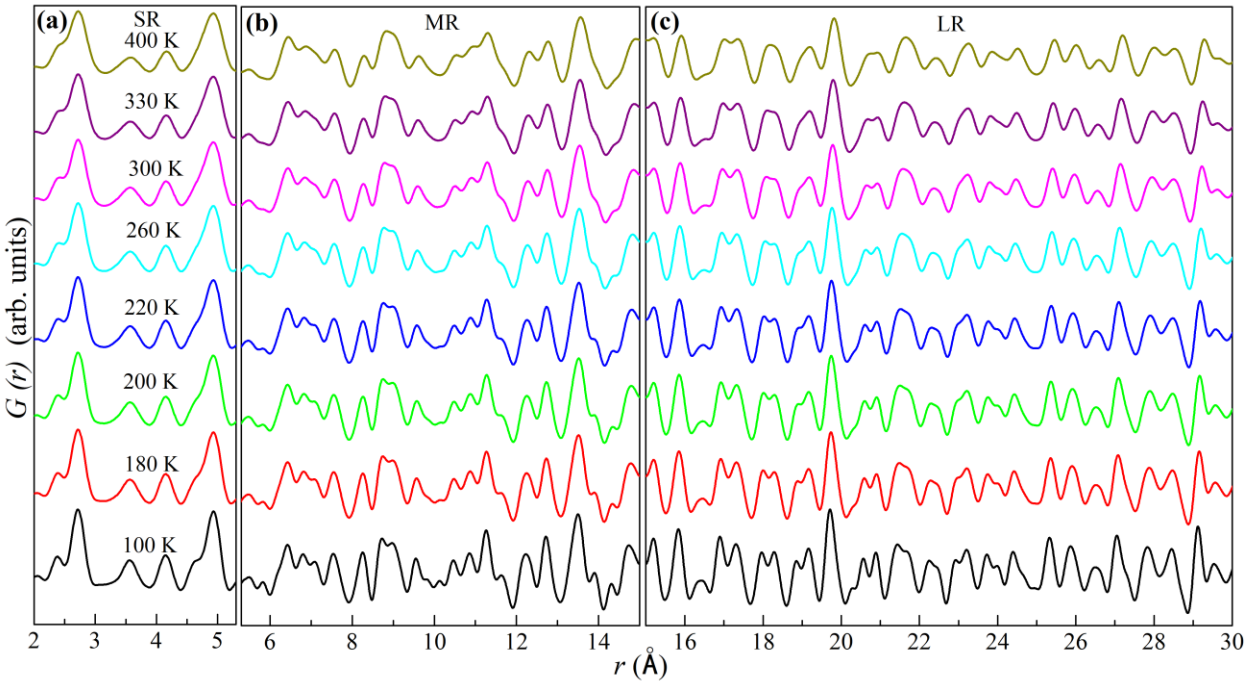

Figure 7.5: Experimental pair distribution functions (PDFs; *G(r)*) on the vertically spaced scale at various temperatures from 400 K to 100 K in the (a) Short-range (SR), (b) Medium-range (MR), and (c) Long-range (LR) regimes.

The reduced atomic PDF *G(r)* has been obtained by taking the Fourier transform of *F(Q)*. The vertically spaced *G(r)* in the SR, MR, and LR regimes in the temperature range of 400-100 K are shown in Figure 7.5(a), (b), and (c), respectively. The effect of temperature on the PDF peak

broadening can be seen for e.g., the PDF peaks around 5 Å, 9 Å, 18 Å, etc. tend to singlet at 400 K from the doublet at 100 K (see Figure 7.5). Apart from the thermal effect, the appearance of any new PDF peak with the change in temperature was not observed. This further confirms the absence of any structural phase transition in the temperature range of 400-100 K.

To get detail insight of the local structure, the real space structure refinements (PDF refinements) were carried out using hexagonal structure ($P6_3/mmc$) at different temperatures. The initial value of lattice parameters, ADPs, and atomic positions was taken from the Rietveld refined crystallographic model structure at the respective temperatures (from Table 7.1). The lattice parameters and ADPs were refined during the PDF refinement. Considering the isotropic ADPs, the results of the PDF refinements at 400 K, 300 K, and 100 K are shown in Figure 7.6(a), (b), and (c), respectively, which reveal that the fittings are good but not the satisfactory (evident by the significant difference PDFs in Figure 7.6(a), (b), and (c)). In contrast, considering the anisotropic ADPs along the basal plane and *c*-direction, the PDF fittings look quite good, as evident by Figure 7.6(d), (e), and (f) for 400 K, 300 K, and 100 K, respectively (see the value of R_w indicated in Figure 7.6(d), (e), and (f)). This suggests the presence of strong anisotropy in the present hexagonal crystal structure of NiMnGa. This is in agreement with the presence of strong uniaxial MCA reported in hexagonal NiMnGa [214]. The parameter obtained after the PDF refinements in the SR to LR at the selected temperatures (400 K, 300 K, and 100 K), covering both magnetic transitions (T_C ~ 350 K and T_{SRT} ~ 200 K), is shown in Table 7.2 and Table 7.3 for isotropic ADPs and anisotropic ADPs consideration, respectively.

Table 7.2: The lattice parameters (*a* and *c*), isotropic atomic displacements parameters (U_{iso}), the coefficient for $1/r^2$ contribution to the peak sharpening (δ_2), and weighted agreement factor (R_w) obtained from the PDF refinement using hexagonal ($P6_3/mmc$ space group) at the selected temperatures of NiMnGa.

Temperature → / Parameters ↓	**400 K**	**300 K**	**100 K**
a (Å)	4.1612(8)	4.1547(7)	4.1451(4)
c (Å)	5.334(1)	5.321(1)	5.295(1)
U_{iso}^{Ni} (Å^2)	0.0091(5)	0.0073(4)	0.0039(2)
U_{iso}^{Mn} (Å^2)	0.0089(4)	0.0072(3)	0.0036(2)
U_{iso}^{Ga} (Å^2)	0.0105(5)	0.0080(4)	0.0041(2)
δ_2 (Å^2)	2.4(5)	2.3(4)	1.9(5)
R_w (%)	13.3	12.5	10.5

Now, looking carefully, the presence of slight misfit observed in the SR in comparison to the LR (see the encircles region of difference PDFs just below 5 Å in Figure 7.6(d), (e), and (f)). To unleash that, the PDF refinements were carried out with the change in distance (*r*-dependent PDF refinement*)* at the different parameters. It is evident from Figure 7.7(a), (b), and (c) that anisotropic ADPs corresponding to Mn changes drastically in the SR region, which is an indication of the local structure distortion. The value thermal parameter (B), obtained using the relation $B = 8\pi^2 U_{33}$, is ~4.34, 2.62, 0.67 Å^2 in the SR (up to $r \sim 5$ Å) at 400 K, 300 K, and 100 K, respectively. Such a large value of B at 400 K and 300 K indicates off-centering of the Mn atom from its original atomic positions in the SR region [410, 413].

Table 7.3: The lattice parameters (*a* and *c*), anisotropic atomic displacements parameters (U_{11} = U_{22} and U_{33}), the coefficient for $1/r^2$ contribution to the peak sharpening (δ_2), and weighted agreement factor (R_w) obtained from the PDF refinement using hexagonal ($P6_3/mmc$ space group) at the selected temperatures of NiMnGa.

Temperature → Parameters ↓	**400 K**	**300 K**	**100 K**
a (Å)	4.1624(7)	4.1553(6)	4.1450(4)
c (Å)	5.336(2)	5.323(2)	5.296(1)
U_{11}^{Ni} (Å^2)	0.0080(6)	0.0061(4)	0.0031(2)
U_{33}^{Ni} (Å^2	0.012(2)	0.010 (1)	0.0072(9)
U_{11}^{Mn} (Å^2)	0.0091(5)	0.0070(4)	0.0036(2)
U_{33}^{Mn} (Å^2)	0.010(2)	0.008(1)	0.0040(6)
U_{11}^{Ga} (Å^2)	0.0061(5)	0.0053(4)	0.0036(2)
U_{33}^{Ga} (Å^2)	0.025(2)	0.018(2)	0.0055(7)
δ_2 (Å^2)	2.5(5)	2.3(4)	1.9(5)
R_w (%)	6.4	7.0	8.1

For better visualization of changes in the SR, the ratio of anisotropic ADPs (U_{33}/U_{11}) of Mn atom at 400 K, 300 K, and 100 K are shown in the inset of Figure 7.7(a), (b), and (c), respectively. A large increase in U_{33}/U_{11} in SR suggests the dominating ADP along *c*-direction as compared to the ADP along the basal plane. Such a large change in the ADPs manifests that the atoms deviate from their Wyckoff positions, which are assigned for the SR during refinement [413]. In addition, the interatomic distances also vary drastically in the SR. These observations suggest that the local structure can differ from the average long-range crystal structure ($P6_3/mmc$) of NiMnGa.

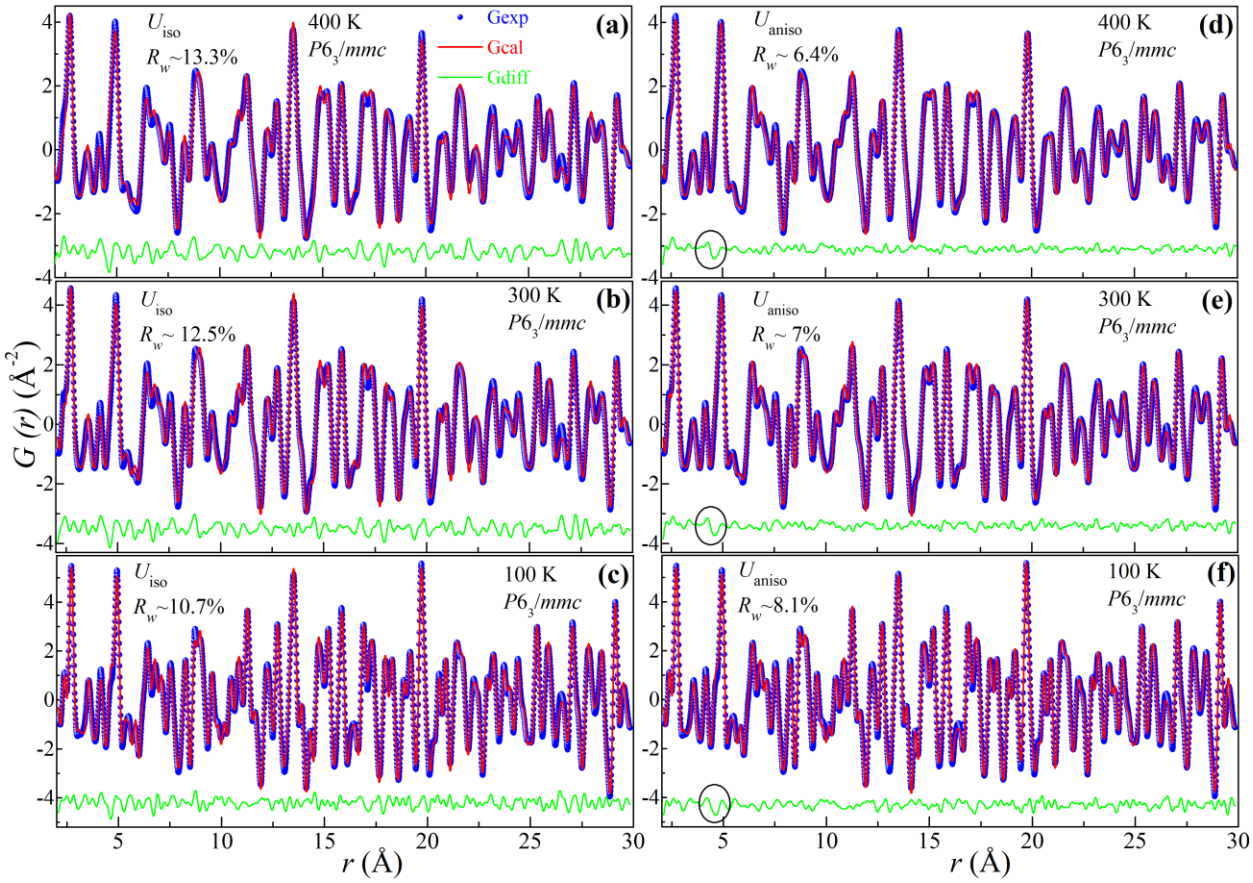

Figure 7.6: The experimental PDF (blue spheres), calculated PDF (continuous red line), their difference (continuous green line at the bottom), and weighted agreement factor (R_w) obtained by real-space structure refinements using the *P*6$_3$*/mmc* space group in the SR and LR at (a) 400 K, (b) 300 K and (c) 100 K with isotropic atomic displacement parameters (ADPs; U_{iso}) consideration in the refinements. The PDFs fits in the SR and LR using the same space group (*P*6$_3$*/mmc*) at (d) 400 K, (e) 300 K, and (f) 100 K with anisotropic ADPs (U_{aniso}) consideration in the refinements. The significant misfit just below 5 Å is indicated by encircled region of difference PDFs (Gdiff) in (d), (e), and (f).

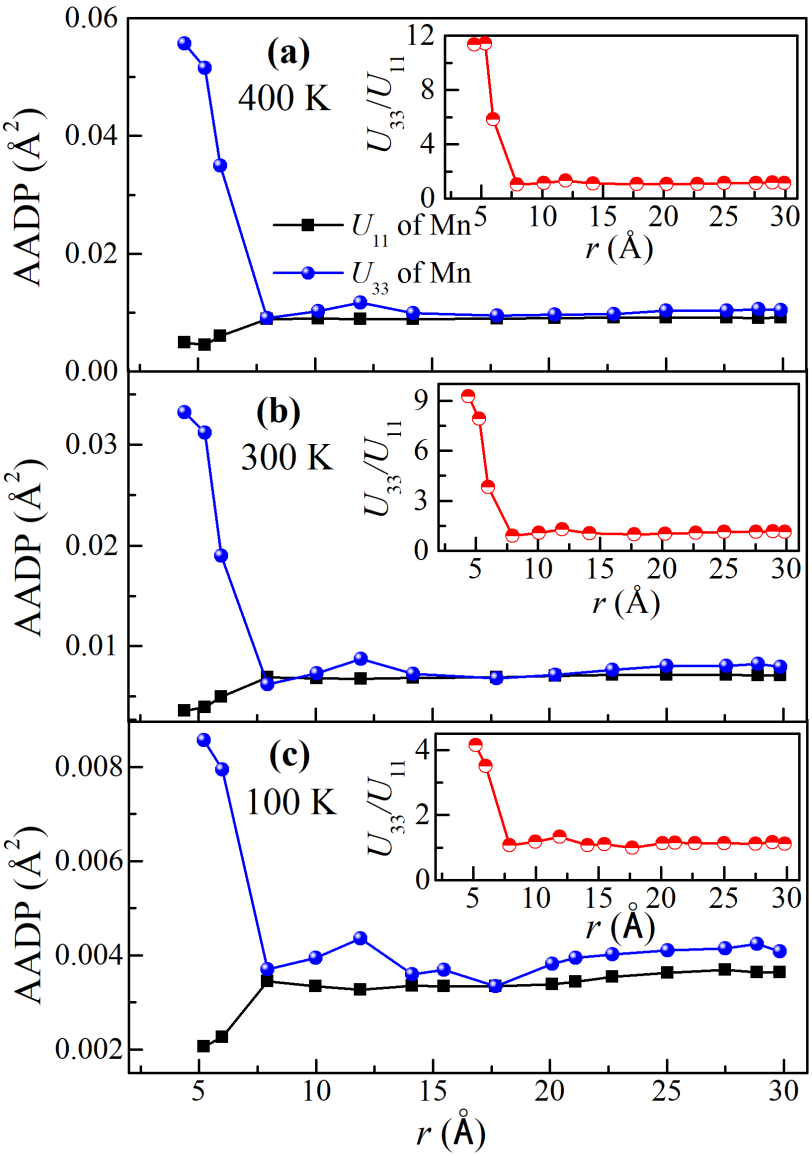

Figure 7.7: The anisotropic atomic displacement parameter (AADP) of the Mn atom with distance (r) obtained after r-dependent real-space structure refinement using the $P6_3/mmc$ space group at (a) 400 K, (b) 300 K, and (c) 100 K. The planer ADP (U_{11}) and prismatic ADP (U_{33}) are indicated by black squares connected with a solid line and blue spheres connected with a solid line, respectively. The insets in the (a), (b), and (c) depict the ratio of U_{33} with U_{11} (i.e., U_{33}/U_{11}) vs r plot.

To investigate the local structure, the different subgroups of $P6_3/mmc$ (194) were considered one by one for the real space structure refinement (PDF refinement). The list of maximal *translationengleiche* type subgroups of $P6_3/mmc$ are $P\bar{6}2c$ (190), $P\bar{6}m2$ (187), $P6_3mc$ (186), $P6_322$ (182), $P6_3/m$ (176), $P\bar{3}m1$ (164), $P\bar{3}1c$ (163), and *Pmmc* (63) [414]. The asymmetric unit of these subgroups are obtained using composition and space group [415] and listed in Table 7.4. Apart from that, *klassengleiche* type subgroups of $P6_3/mmc$ are $P6_3/mmc$ with enlarged or modulated unit cell, e.g., $c'=3c$; $a'=3a$, $b'=3b$; $a'=2a$, $b'=2b$; and $P6_3/mcm$ (193), where, a', b', c' and a, b, c are cell parameters of the enlarged and basic unit cell, respectively [414].

In the main $P6_3/mmc$, all the atoms are occupied their special Wyckoff positions, i.e., Mn at 2a (0, 0, 0), Ni at 2d (1/3, 2/3, 3/4), and Ga at 2c (1/3, 2/3, 1/4) with total six number of atoms per formula unit (or asymmetric unit) of NiMnGa [187, 214]. The PDF fitting using $P6_3/mmc$ space group in the SR at 300 K is shown in Figure 7.8(a), which reveals a significant misfit around 3.5 Å with R_w ~11.4%. In order to get the better structural model, the PDF refinements were carried out using each subgroup of $P6_3/mmc$, and the result of the refinements are shown in Figure 7.8(b)-(h) and (j) in the SR at 300 K. The lattice parameters, isotropic ADPs, and suitable atomic positions were varied during the PDF refinement. Since the asymmetric unit of $P\bar{6}2c$, $P6_322$, $P6_3/m$, and $P\bar{3}1c$ contains Wyckoff positions similar to $P6_3/mmc$ (see Table 7.4**)**; they provide similar fitting as of $P6_3/mmc$ (see Figure 7.8(a) and (d)-(g)). This suggests that $P\bar{6}2c$, $P6_322$, $P6_3/m$, and $P\bar{3}1c$ do not belong to a suitable lower symmetry space group. Since the asymmetric unit of $P\bar{6}m2$, $P6_3mc$, and *Pmmc* contain refinable Wyckoff position (see Table 7.4**)**, they provide a slightly better fit in comparison to $P6_3/mmc$ (see Figure 7.8(a)-(c) and (h)). Although, the fitting from these subgroups ($P\bar{6}m2$, $P6_3mc$, and *Pmmc*) looks good, a further possibility was investigated to achieve the best fit. The consideration of *klassengleiche* type subgroups with enlarged unit cells in the $P6_3/mmc$

and $P6_3/mcm$ were also failed to provide a good fit to the experimental PDF. In addition, the possibility of additional space group *Pnma*, which is orthorhombic martensite phase from hexagonal austenite phase observed in *MnM′X* class of materials (see the detailed discussion in section 6.1) [196], were also discarded as this space group (*Pnma*) provides a bad fit to the experimental PDF with $R_w \sim 18.7\%$ as shown in Figure 7.8(i).

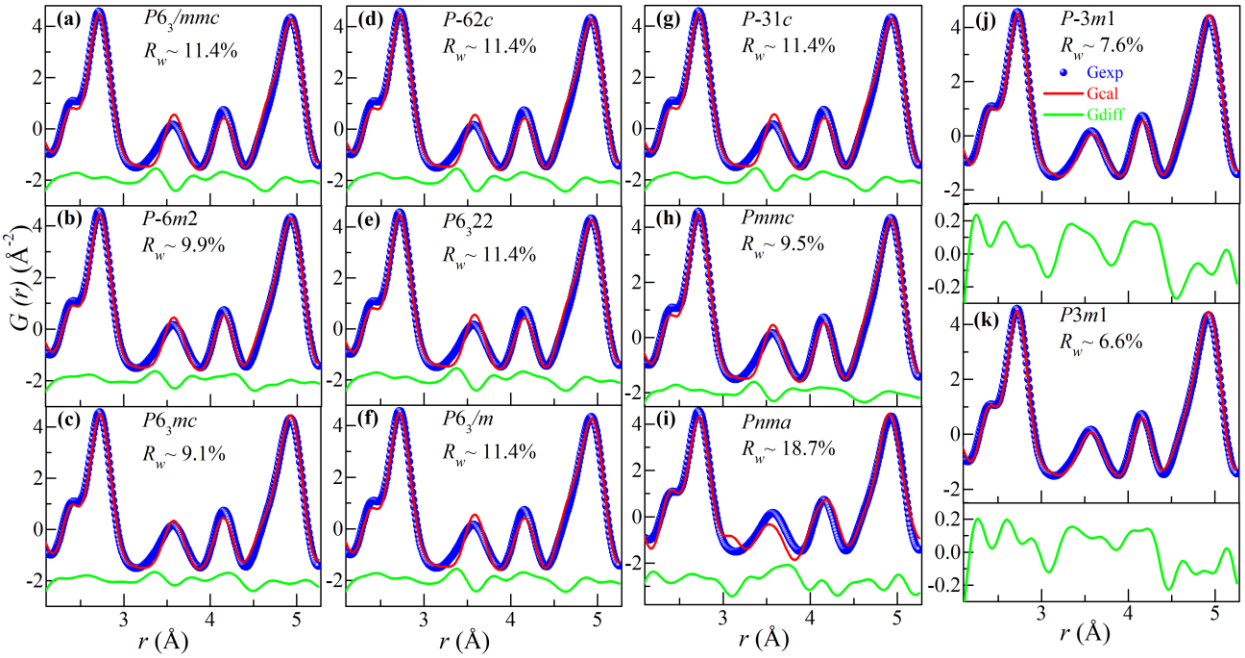

Figure 7.8: The experimental PDF (blue spheres), calculated PDF (continuous red line), their difference (continuous green line at the bottom), and weighted agreement factor (R_w) obtained by real-space structure refinements in the SR at 300 K using space group (a) $P6_3mmc$, (b) $P\bar{6}m2$, (c) $P6_3mc$, (d) $P\bar{6}2c$, (e) $P6_322$, (f) $P6_3/m$, (g) $P\bar{3}1c$, (h) *Pmmc*, (i) *Pnma*, (j) $P\bar{3}m1$, and (k) $P3m1$. For comparison, the difference PDF (Gdiff) of (j) and (k) are depicted in separate panels given below (j) and (k), respectively.

Among all the subgroups, it is found that the $P\bar{3}m1$ provides an excellent fit to the experimental PDF with $R_w \sim 7.6\%$, as shown in Figure 7.8(j). Interestingly, PDF refinement using another lower symmetry space group, $P3m1$, which has been reported for sister compound PtMnGa [209], is

found to provide an even better fit than $P\bar{3}m1$. The result of the PDF refinement using the $P3m1$ space group is shown in Figure 7.8(k), which reveals the best fit with $R_w \sim 6.6\%$. For comparison, the difference PDF (Gdiff), obtained after the PDF refinement using $P\bar{3}m1$ and $P3m1$ are shown in the separate panels below Figure 7.8(j) and below Figure 7.8(k), respectively. It is evident from Figure 7.8(j) and Figure 7.8(k) that Gdiff using $P\bar{3}m1$ is larger than Gdiff using $P3m1$ (see the range of $r \sim 3.14$ to 4.4 Å in the Gdiff of Figure 7.8(j) and Figure 7.8(k)). Thus, after the trial of several space groups in the PDF refinement, the $P3m1$ space group symmetry was found to be the most suitable lower symmetry structure to model the experimental PDF. This suggests that the local short-range structure of NiMnGa is trigonal with $P3m1$ space group symmetry at 300 K.

Table 7.4: List of subgroups of $P6_3/mmc$ (194), their asymmetric unit, Wyckoff positions [415], and weighted agreement factor (R_w) of the real-space structure refinement of NiMnGa. The $P6_3/mmc$ (194) is not the subgroup. It is added just given for the comparison of Wyckoff positions and R_w.

Subgroups of $P6_3/mmc$ (194)	**Asymmetric unit**	**Wyckoff Positions** ***(To indicate the refinable atomic positions)***	**R_w (%)**
$P6_3/mmc$ (194)		Mn: 2a (0, 0, 0) (0, 0, 1/2) Ni: 2d (1/3, 2/3, 3/4) (2/3, 1/3, 1/4) Ga: 2c (1/3, 2/3, 1/4) (2/3, 1/3, 3/4)	11.4
$P\bar{6}2c$ (190)	Mn: 2a (0, 0, 0) (0, 0, 1/2) Ni: 2d (1/3, 2/3, 3/4) (2/3, 1/3, 1/4) Ga: 2c (1/3, 2/3, 1/4) (2/3, 1/3, 3/4)	Mn: 2a (0, 0, 0) (0, 0, 1/2) Ni: 2d (1/3, 2/3, 3/4) (2/3, 1/3, 1/4) Ga: 2c (1/3, 2/3, 1/4) (2/3, 1/3, 3/4)	11.4
$P\bar{6}m2$ (187)	Mn: 2g (0, 0, 3/4) (0, 0, 1/4) Ni1: 1d (1/3, 2/3, 1/2) Ni2: 1e (2/3, 1/3, 0) Ga1: 1c (1/3, 2/3, 0) Ga2: 1f (2/3, 1/3, 1/2)	Mn: 2g (0, 0, z) (0, 0, -z) Ni1: 1d (1/3, 2/3, 1/2) Ni2: 1e (2/3, 1/3, 0) Ga1: 1c (1/3, 2/3, 0) Ga2: 1f (2/3, 1/3, 1/2)	9.9

$P6_3mc$ (186)	Mn: 2a (0, 0, 0) (0, 0, 1/2) Ni: 2b (1/3, 2/3, 3/4) (2/3, 1/3, 1/4) Ga: 2b (1/3, 2/3, 1/4) (2/3, 1/3, 3/4)	Mn: 2a (0, 0, z) (0, 0, z+1/2) Ni: 2b (1/3, 2/3, z) (2/3, 1/3, z+1/2) Ga: 2b (1/3, 2/3, z) (2/3, 1/3, z+1/2)	9.1
$P6_322$ (182)	Mn: 2a(0, 0, 0)(0, 0, 1/2) Ni: 2d (1/3, 2/3, 3/4) (2/3, 1/3, 1/4) Ga: 2c (1/3, 2/3, 1/4) (2/3, 1/3, 3/4)	Mn: 2a(0, 0, 0)(0, 0, 1/2) Ni: 2d (1/3, 2/3, 3/4) (2/3, 1/3, 1/4) Ga: 2c (1/3, 2/3, 1/4) (2/3, 1/3, 3/4)	11.4
$P6_3/m$ (176)	Mn: 2b (0, 0, 0) (0, 0, 1/2) Ni: 2d (1/3, 2/3, 3/4) (2/3, 1/3, 1/4) Ga: 2c (1/3, 2/3, 1/4) (2/3, 1/3, 3/4)	Mn: 2b (0, 0, 0) (0, 0, 1/2) Ni: 2d (1/3, 2/3, 3/4) (2/3, 1/3, 1/4) Ga: 2c (1/3, 2/3, 1/4) (2/3, 1/3, 3/4)	11.4
$P\bar{3}m1$ (164)	Mn1: 1a (0, 0, 0) Mn2: 1b (0, 0, 1/2) Ni: 2d (1/3, 2/3, 3/4) (2/3, 1/3, 1/4) Ga: 2d (1/3, 2/3, 1/4) (2/3, 1/3, 3/4)	Mn1: 1a (0, 0, 0) Mn2: 1b (0, 0, 1/2) Ni: 2d (1/3, 2/3, z) (2/3, 1/3, -z) Ga: 2d (1/3, 2/3, z) (2/3, 1/3, -z)	7.6
$P\bar{3}1c$ (163)	Mn: 2b (0, 0, 0)(0, 0, 1/2) Ni: 2d (1/3, 2/3, 3/4) (2/3, 1/3, 1/4) Ga: 2c (1/3, 2/3, 1/4) (2/3, 1/3, 3/4)	Mn: 2b (0, 0, 0)(0, 0, 1/2) Ni: 2d (1/3, 2/3, 3/4) (2/3, 1/3, 1/4) Ga: 2c (1/3, 2/3, 1/4) (2/3, 1/3, 3/4)	11.4
Pmmc (63)	Mn: 4a (0, 0, 0) (0, 0, 1/2) Ni: 4c (0, 2/3, 1/4) (0, 1/3, 3/4) (1/2, 0.16, 1/4) (1/2, 0.83, 3/4) Ga: 4c (0, 2/3, 3/4) (0, 1/3, 1/4)	Mn: 4a (0, 0, 0) (0, 0, 1/2) Ni: 4c (0, y, 1/4) (0, -y, 3/4) Ga: 4c (0, y, 1/4) (0, -y, 3/4)	9.5
Additional space groups			
$P3m1$ (156) [209]	Mn1: 1a (0, 0, 0) Mn2: 1a (0, 0, 1/2) Ni1: 1b (1/3, 2/3, 3/4) Ni2: 1c (2/3, 1/3, 1/4) Ga1: 1b (1/3, 2/3, 1/4) Ga2: 1c (2/3, 1/3, 3/4)	Mn1: 1a (0, 0, z) Mn2: 1a (0, 0, z) Ni1: 1b (1/3, 2/3, z) Ni2: 1c (2/3, 1/3, z) Ga1: 1b (1/3, 2/3, z) Ga2: 1c (2/3, 1/3, z)	6.6
Pnma (62) [196]		Mn: 4c (x, 1/4, z) (-x, 3/4, -z), (1/2-x, 3/4, 1/2+z), (1/2+x, 3/4, 1/2-z) Ni: 4c Ga: 4c	18.7

Table 7.5: The lattice parameters (*a* and *c*), isotropic atomic displacements parameters (U_{iso}), coefficient for $1/r^2$ contribution to the peak sharpening (δ_2), atomic positions and weighted agreement factor (R_w) obtained from the PDF refinement in the SR using trigonal structure with *P*3*m*1 space group at the selected temperatures of NiMnGa.

Temperature → Parameters ↓	**400 K**	**300 K**	**100 K**
a (Å)	4.163(4)	4.158(2)	4.149(1)
c (Å)	5.326(3)	5.312(5)	5.299(2)
U_{iso}^{Ni} (Å^2)	0.011(3)	0.006(3)	0.004(4)
U_{iso}^{Mn} (Å^2)	0.006(4)	0.005(3)	0.004(1)
U_{iso}^{Ga} (Å^2)	0.009(2)	0.007(2)	0.003(3)
Position of Ni1	1b (1/3, 2/3, 0.726 (5))	1b (1/3, 2/3, 0.724(6))	1b (1/3, 2/3, 0.744(4))
Position of Ni2	1c (2/3, 1/3, 0.261(3))	1c (2/3, 1/3, 0.256(4))	1c (2/3, 1/3, 0.262(2))
Position of Mn1	1a (0, 0, 0.035(1))	1a (0, 0, 0.024(2))	1a (0, 0, 0.022(1))
Position of Mn2	1a (0, 0, 0.511(4))	1a (0, 0, 0.505(6))	1a (0, 0, 0.512(3))
Position of Ga1	1b (1/3, 2/3, 0.255(2))	1b (1/3, 2/3, 0.250(5))	1b (1/3, 2/3, 0.253(2))
Position of Ga2	1c (2/3, 1/3, 0.761(7))	1c (2/3, 1/3, 0.756(8))	1c (2/3, 1/3, 0.764(4))
δ_2 (Å^2)	3.5(6)	2.9(6)	2.1(7)
R_w (%)	6.2	6.6	7.5

As NiMnGa exhibits paramagnetic to ferromagnetic (FM) phase transition at $T_C \sim 350$ K and FM to spin reorientation transition (SRT) transition at $T_{SRT} \sim 200$ K (see Figure 7.1), it is interesting to see the stability of the present local structure ($P3m1$) of NiMnGa with change in temperature. The SR structure (trigonal with $P3m1$ space group) in the FM phase ($T_C > 300$ K $> T_{SRT}$) is already obtained (see Figure 7.8(k)). The comparison of PDF refinement using $P6_3/mmc$ and $P3m1$space groups in the SR at 400 K and 100 K are shown in Figure 7.9(a-d). The parameters obtained from the PDF refinements at the selected temperatures in the SR using the $P3m1$ space group are given in

Table *7.5*. The PDF refinement in the paramagnetic phase at 400 K ($T_C < 400$ K) provides better fit with $P3m1$ (shown in Figure 7.9(b) with $R_w \sim 6.2\%$) in comparison to $P6_3/mmc$ (shown in Figure 7.9(a), with $R_w \sim 11.8\%$). This suggests that the trigonal structure with $P3m1$space group symmetry present in the SR at 400 K. Further, the PDF refinement in the SRT phase at 100 K ($T_{SRT} > 100$ K) provides the better fit with $P3m1$ (see Figure 7.9(d), $R_w \sim 7.5\%$) in comparison to $P6_3/mmc$ (see Figure 7.9(c), $R_w \sim 10.5\%$). This suggests that the trigonal structure with $P3m1$space group symmetry present in the SR even at 100 K. All these results suggest that the SR trigonal structure of NiMnGa with $P3m1$space group is stable from 400 to 100 K.

We also compared the long-structure (LR) structure of NiMnGa using the $P3m1$ space group with $P6_3/mmc$ space group at different temperatures (covering both the magnetic phase transition, i.e., T_C and T_{SRT}). The comparison of PDF refinements using $P6_3/mmc$ and $P3m1$space groups in the LR range at 400 K and 100 K are shown in Figure 7.9(e)-(h). A better fit between experimental and calculated PDFs is observed for $P6_3/mmc$ (see Figure 7.9(e), $R_w \sim 13.1\%$) in comparison to

*P*3*m*1 (see Figure 7.9(f), R_w ~ 16.2%) at 400 K in the LR. Further, such a better fit is observed down to 100 K for *P*6$_3$/*mmc* (see Figure 7.9(g), R_w ~ 10.6%) in comparison to *P*3*m*1 (see Figure 7.9(h), R_w ~ 14.3%) in the LR. Further, the Rietveld refinements, shown in Figure 7.4(a)-(c), clearly reveal that the average long-range structure of NiMnGa is hexagonal with *P*6$_3$/*mmc* space group. Thus, the local SR structure is trigonal with the *P*3*m*1 space group, while the average LR structure remains hexagonal with *P*6$_3$*mmc* space group of NiMnGa compound.

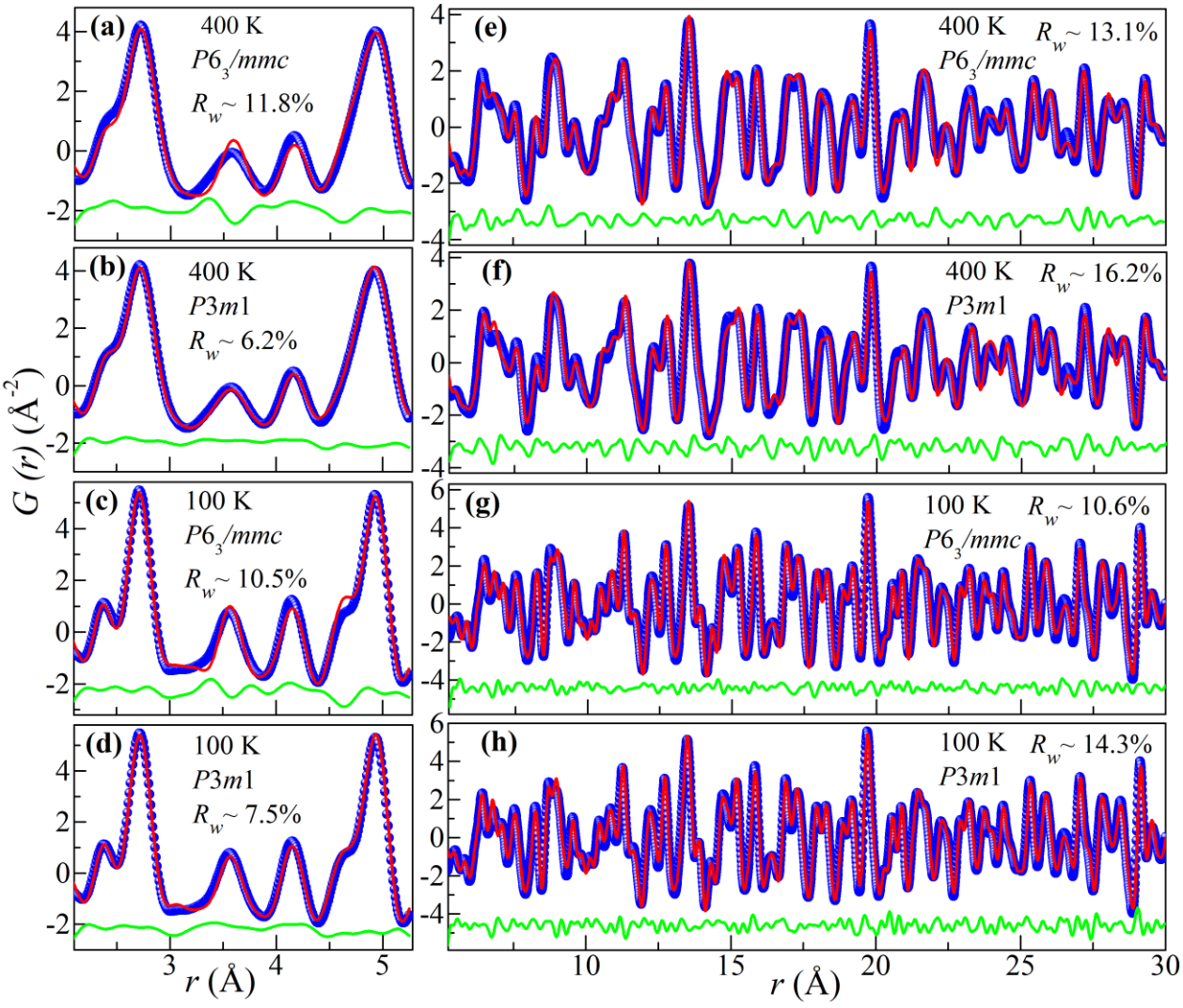

Figure 7.9: The experimental PDF (blue spheres), calculated PDF (continuous red line), their difference (continuous green line at the bottom), and weighted agreement factor (R_w) obtained by

real-space structure refinements using the $P6_3/mmc$ space group in the SR at (a) 400 K and (c) 100 K, while in the LR at (e) 400 K and (g) 100 K. The PDFs fits using the $P3m1$ space group in the SR at (b) 400 K and (d) 100 K, while in the LR at (f) 400 K and (h) 100 K.

It is worth mentioning here that $P6_3/mmc$ is centrosymmetric, while $P3m1$is a noncentrosymmetric space group. It is well known that the origin of skyrmions critically depends on the inversion symmetry of the crystal structure present in the noncentrosymmetric materials [232]. The presence of DMI in materials with noncentrosymmetric crystal structures has been proposed as a key factor for the origin of skyrmions [232]. In contrast, the origin of skyrmions in materials with centrosymmetric crystal structure has remained debatable due to the absence of the DMI [187, 233, 403]. A recent theoretical study proposes that the skymions can be stabilized in the globally centrosymmetric material by local DMI, induced by breaking of inversion symmetry locally [416]. Further, the biskymions has also been observed in the noncentrosymmetric material ($Cr_{11}Ge_{19}$) [404]. Therefore, on the basis of the PDF analysis, we argue that the presence of local noncentrosymmetric trigonal structure (with $P3m1$ space group) induces local DMI in NiMnGa, which stabilizes the biskymions in the centrosymmetric ($P6_3/mmc$) NiMnGa compound.

7.4 Conclusions

Temperature dependent ac-susceptibility measurement confirms magnetic phase transitions in NiMnGa. Magnetic field-dependent ac-susceptibility measurement revealed the skyrmion state with hysteretic character stabled down to 5 K, and the critical field for skymion formation gets enhanced on lowering the temperature. Rietveld refinements using high-Q PDF data reveal that the average LR hexagonal ($P6_3/mmc$) structure remains unchanged with the change in temperature in the 400-100 K range. The PDF analysis reveals that anisotropic ADPs consideration provides

better fits to the experimental PDF in comparison to the isotropic ADPs, but the large value of anisotropic ADPs observed in the SR at all the respective temperatures. A careful analysis in the SR unleashes the presence of trigonal structure with noncentrosymmetric space group *P*3*m*1. The present results of local noncentrosymmetric structure open a new pathway to revisit the origin of skyrmions in the materials with the centrosymmetric crystal structure.